NeuroImage 208 (2020) 116415

Contents lists available at ScienceDirect

NeuroImage

journal homepage: www.elsevier.com/locate/neuroimage

Longitudinal evaluation of demyelinated lesions in a multiple sclerosis model using ultrashort echo time magnetization transfer (UTE-MT) imaging

Caroline Guglielmetti [a,b,c], Tanguy Boucneau [b], Peng Cao [b], Annemie Van der Linden [c], Peder E.Z. Larson [b,d], Myriam M. Chaumeil [a,b,d,*]

[a] Department of Physical Therapy and Rehabilitation Science, University of California, San Francisco, CA, USA
[b] Department of Radiology and Biomedical Imaging, University of California, San Francisco, CA, USA
[c] Bio-Imaging Laboratory, Department of Biomedical Sciences, University of Antwerp, 2000, Antwerp, Belgium
[d] UC Berkeley-UCSF Graduate Program in Bioengineering, Berkeley and University of California, San Francisco, CA, USA

ARTICLE INFO

Keywords:
Ultrashort echo time
Magnetization transfer
Myelin
Demyelination
Multiple sclerosis
Cuprizone

ABSTRACT

Alterations in myelin integrity are involved in many neurological disorders and demyelinating diseases, such as multiple sclerosis (MS). Although magnetic resonance imaging (MRI) is the gold standard method to diagnose and monitor MS patients, clinically available MRI protocols show limited specificity for myelin detection, notably in cerebral grey matter areas. Ultrashort echo time (UTE) MRI has shown great promise for direct imaging of lipids and myelin sheaths, and thus holds potential to improve lesion detection.

In this study, we used a sequence combining magnetization transfer (MT) with UTE ("UTE-MT", TE = 76 μs) and with short TE ("STE-MT", TE = 3000 μs) to evaluate spatial and temporal changes in brain myelin content in the cuprizone mouse model for MS on a clinical 7 T scanner. During demyelination, UTE-MT ratio (UTE-MTR) and STE-MT ratio (STE-MTR) values were significantly decreased in most white matter and grey matter regions. However, only UTE-MTR detected cortical changes. After remyelination in subcortical and cortical areas, UTE-MTR values remained lower than baseline values, indicating that UTE-MT, but not STE-MT, imaging detected long-lasting changes following a demyelinating event.

Next, we evaluated the potential correlations between imaging values and underlying histopathological markers. The strongest correlation was observed between UTE-MTR and percent coverage of myelin basic protein (MBP) immunostaining ($r^2 = 0.71$). A significant, although lower, correlation was observed between STE-MTR and MBP ($r^2 = 0.48$), and no correlation was found between UTE-MTR or STE-MTR and gliosis immunostaining. Interestingly, correlations varied across brain substructures.

Altogether, our results demonstrate that UTE-MTR values significantly correlate with myelin content as measured by histopathology, not only in white matter, but also in subcortical and cortical grey matter regions in the cuprizone mouse model for MS. Readily implemented on a clinical 7 T system, this approach thus holds great potential for detecting demyelinating/remyelinating events in both white and grey matter areas in humans. When applied to patients with neurological disorders, including MS patient populations, UTE-MT methods may improve the non-invasive longitudinal monitoring of brain lesions, not only during disease progression but also in response to next generation remyelinating therapies.

1. Introduction

Myelin is an essential component of the central nervous system (CNS) that ensures proper neuronal function and neural transmission (Baumann and Pham-Dinh, 2001). Alterations and damage of the myelin sheaths have been implicated in various neurological disorders, particularly multiple sclerosis (MS) (Love, 2006; Popescu and Lucchinetti, 2012; Reich et al., 2018). MS is an autoimmune disease that leads to demyelination in the CNS, both in white and grey matter areas, resulting in motor and cognitive disabilities. Patients suffering from MS present brain lesions characterized by demyelination and presence of inflammatory cells (Reich et al., 2018). Magnetic resonance imaging (MRI) is the preferred imaging tool for diagnosis of MS and monitoring of disease activity and progression. Although conventional MRI techniques have

* Corresponding author. 1700 4th Street, BH 204 Mission Bay Campus Box 2530, San Francisco, CA, 94143, USA.
E-mail address: myriam.chaumeil@ucsf.edu (M.M. Chaumeil).

https://doi.org/10.1016/j.neuroimage.2019.116415
Received 16 September 2019; Received in revised form 16 November 2019; Accepted 28 November 2019
Available online 4 December 2019

demonstrated very high sensitivity for the detection of lesions in white matter and active lesions associated with a leaky blood brain barrier (Filippi and Rocca, 2011; Filippi et al., 2016; Traboulsee et al., 2016), to date, there is still a lack of robust methods that allow detecting lesions located in grey matter and cortical areas. Therefore, development and validation of novel MRI methods enabling non-invasive evaluation of myelin integrity would not only provide new tools to improve our understanding of MS pathology, but are also becoming a necessity as novel drugs promoting tissue repair and remyelination are underway (Green et al., 2017; Plemel et al., 2017).

In the CNS, myelin is a specialized structure sheathing the axons, and is constituted by spirally wrapped membranes originating from oligodendrocytes. This multilamellar structure is principally composed of lipids (70% of dry weight) and myelin-associated proteins (Baumann and Pham-Dinh, 2001). Due to this unique arrangement, myelin lipid protons and protons in water molecules that are tightly bound to myelin possess very short T_2 relaxation times, in the order of 50–1000μs, that cannot be detected with conventional clinical magnetic resonance (MR) sequences (Horch et al., 2011; Laule et al., 2007; Wilhelm et al., 2012).

Several MR-based strategies have been developed to indirectly image myelin, such as T_2 relaxometry and measure of myelin water fraction, diffusion tensor and diffusion kurtosis MR imaging, and magnetization transfer (MT) imaging. For extensive review of these MR techniques and their applications to myelin imaging, we refer the reader to (Heath et al., 2018; Laule et al., 2007; Ontaneda and Fox, 2017). Over the past decade, a number of studies have brought evidences that very short T_2 components associated with myelin lipids could be imaged using ultra-short echo time (UTE) MRI sequences (Boucneau et al., 2018; Du et al., 2014; Fan et al., 2017, 2018; He et al., 2017; Horch et al., 2011; Robson et al., 2003; Sheth et al., 2016, 2017; Wilhelm et al., 2012). Recently, UTE sequences have been combined with magnetization transfer (MT) techniques for the assessment of tissue possessing extremely short T_2 relaxation times (Carl et al., 2018; Chang et al., 2015a; Du et al., 2009; Hodgson et al., 2011; Wei et al., 2018). In short, an off-resonance radiofrequency pulse is applied before the standard UTE sequence in order to sensitize the MR signal to proton pools with extremely short T_2 relaxation times. From these UTE-MT sequences, quantitative UTE-MT ratio (UTE-MTR) values can be obtained, that reflect both direct saturation of ultrashort T_2 components as well as MT saturation of longer T_2 components. To date, UTE-MTR measures have shown great promises for differentiating between normal control and pathological abnormalities of tendons, cortical bones, and more recently, for improving the characterization of tissue microstructure in the human brain (Chang et al., 2015a, 2015b; Grosse et al., 2013; Syha et al., 2014; Wei et al., 2018).

The cuprizone (CPZ) mouse model is a well-described and very reproducible animal model of MS, which makes it highly suitable for validation of imaging techniques (Guglielmetti et al., 2017a; Matsushima and Morell, 2001; Nathoo et al., 2014; Praet et al., 2014). Supplementation of regular rodent diet with 0.2% of the copper chelator CPZ has been shown to induce oligodendrocyte cell death, demyelination and important reactive gliosis in the forebrain and cerebellum (Groebe et al., 2009; Kipp et al., 2009; Skripuletz et al., 2008, 2010). Both white and grey matter, including subcortical and cortical grey areas, undergo severe demyelination within a few weeks of CPZ administration. Interestingly, when CPZ is withdrawn from the diet, spontaneous remyelination occurs (Matsushima and Morell, 2001). Additionally, studies have reported that the degree of demyelination varies within white matter areas, in particular along the rostro-caudal plane, thus enabling to evaluate the relative sensitivity of imaging tools to disease severity (Guglielmetti et al., 2016b; Steelman et al., 2012; Tagge et al., 2016; Wu et al., 2008; Xie et al., 2010).

In this study, we evaluated the potential of a UTE-MT MR sequence to generate images with high contrast for cerebral structures in the mouse brain using a clinical 7 T MRI scanner. We also acquired images using a short TE (STE) within the same MR acquisition scheme, for comparison and paired assessment of the effect of TE on the image contrast. Next, we conducted a longitudinal imaging study to examine the temporal changes of UTE-MTR and STE-MTR following CPZ-mediated brain demyelination, gliosis, and subsequent remyelination. Our results indicated that UTE-MTR and STE-MTR can detect CPZ-induced alterations in white matter and subcortical grey matter, while only UTE-MTR detected alterations in cortical grey matter during the demyelination phase. At the end of the recovery period, UTE-MTR could detect spontaneous remyelination in white matter and persistent changes to tissue microstructure in subcortical and cortical grey areas, while STE-MTR only detected spontaneous remyelination in the white matter. Importantly, we also showed that UTE-MTR was more strongly associated with myelin content as assessed by histopathology, as compared to STE-MTR. Altogether, our findings demonstrated that UTE-MT imaging can detect brain tissue alterations in white and grey matter in the CPZ model for MS. This MR approach is readily clinically translatable, and thus has great potential to improve characterization of damaged tissue at acute and chronic time points in MS patients.

2. Materials and methods

2.1. Animals and experimental outline

All animal research was approved by the Institutional Animal Care and Use Committee of the University of California, San Francisco. B6(Cg)-Tyr^{c-2J}/J (stock no. 000058) albino female mice (n = 30) were purchased from Jackson Laboratories (Bar Harbor, ME, USA). At eight weeks of age, all mice received a 0.2% cuprizone (CPZ, Sigma-Aldrich) diet for up to six weeks to induce cerebral demyelination. At the end of the six-week period, mice were returned to a standard rodent chow for an additional period of six weeks to allow for recovery and remyelination, as previously described (Guglielmetti et al., 2016b, 2017b).

A total of six mice underwent longitudinal MRI exams at eight weeks of age, prior to CPZ administration (W0, Control), after four weeks of CPZ diet (W4 CPZ), after six weeks of CPZ diet (W6 CPZ), and after six weeks of CPZ diet followed by six weeks of recovery (W6 CPZ + W6 recovery). A separate group of mice (n = 24 mice) that was not subject to any MRI was euthanized at each corresponding imaging time point (n = 6 mice per time point) in order to perform quantitative immunofluorescence analyses.

2.2. MRI acquisitions

In vivo imaging experiments were conducted on a 7 T human imaging system (MR950, GE Healthcare, Waukesha, WI) equipped with 50 mT/m, 200 mT/m/ms gradients and a ^{1}H home-build transmit/receive surface coil (Ø = 20 mm). For each imaging session, mice were anesthetized using isoflurane (1.5–2% in O_2) and placed in a dedicated water-heated cradle allowing for reproducible positioning of the mouse head.

Acquisition of the 3D UTE and STE gradient-echo MRI data were performed within the same sequence with the following parameters: repetition time (TR) = 20 ms, echo time (TE_1) = 76 μs (for UTE), TE_2 = 3000 μs (for STE), flip angle = 10°, non-selective hard pulse excitation, field-of-view (FOV) 17 × 12.5 × 22 mm^3, total readout length 1320 μs, 4 averages, voxel sixe = 200 × 200 × 500 μm^3. The readout bandwidth was ±125 kHz, and approximately 40,000 spokes were acquired per image. The sequence used a 3D radial k-space trajectory supporting anisotropic field-of-view and resolution. An analytic density compensation was applied based on the k-space trajectory (Larson et al., 2008). Images were reconstructed using gridding. To create the magnetization transfer contrast, UTE and STE images were acquired two ways: with an off-resonance radio frequency (RF) pulse incorporated into the sequence (saturated), and without the off-resonance RF pulse (unsaturated). The RF saturation scheme used a pair of adiabatic hyperbolic secant (sech) 180° pulses with a total pulse length = 20 ms, pulse bandwidth = 1 kHz, and nominal peak power = 0.15 G, which was applied at the offset frequency of −1800 Hz from water; each saturation pulse was followed by 8

repetitions. The total scan time for both saturated and unsaturated acquisitions was approximately 40 min.

2.3. MRI post-processing and analysis

Magnetization transfer ratio (MTR) maps were reconstructed with custom-built programs written in MATLAB (Matlab, 2015b; The MathWorks) using the following formula based on the unsaturated and saturated images: $M_{MTR} = (|M_{unsaturated}| - |M_{saturated}|)/|M_{unsaturated}|$. UTE-MTR maps were generated using images acquired with $TE_1 = 76$ μs, and STE-MTR maps using images acquired with $TE_2 = 3000$ μs, as illustrated in Supplementary Fig. 1.

Regions of interest (ROIs) were manually delineated using AMIRA software (Mercury Computer systems, San Diego, USA) on the UTE-MTR maps, and the mean UTE-MTR value was calculated for each ROI. The ROIs delineated on the UTE-MTR maps were then propagated to the STE-MTR maps to obtain the corresponding mean STE-MTR values. In order to minimize partial volume effect, we delineated small ROIs over four to five consecutives axial UTE-MTR map slices, so the total volume per area was equal or exceeded 0.36 mm^3. ROIs were delineated at two distinct brain locations (Bregma +0.6 mm and Bregma -2mm) as indicated in Supplementary Fig. 2. The following ROIs were delineated: 1) three white matter tracts regions: splenium of the corpus callosum, genu of the corpus callosum, and internal capsule; 2) three subcortical areas: thalamus, caudate/putamen, and hippocampus; 3) three cortical areas: retrospinal cortex, somatosensory cortex and motor cortex.

2.4. Histological analyses

Histological analyses were performed as previously described (Guglielmetti et al., 2017b). Briefly, mice were intracardially perfused with a phosphate buffered saline (PBS) solution followed by a 4% paraformaldehyde (PFA) solution. Next, brains were dissected and postfixed in a 4% PFA solution for 24 h, then dehydrated through a sucrose gradient (2 h at 5%, 2 h at 10%, and overnight at 20%). Afterwards, brain tissue was snap-frozen in liquid nitrogen and kept at - 80 °C until further processing. Ten μm-thick cryosections were collected using a cryostat microtome (Leica, CM1850). The presence of myelin was qualitatively assessed with Black-Gold II histochemical staining, as Black-Gold II stain distributes in the inner, compact and outer myelin layers (Savaskan et al., 2009; Schmued et al., 2008). Quantitative analyses of myelin content were evaluated using myelin basic protein (MBP) immunofluorescence, as previously described (Guglielmetti et al., 2016b). For Black-Gold II staining, the sections were incubated in Black-Gold II solution at 60 °C for twelve to fourteen minutes, rinsed in H_2O, and incubated in 1% sodium thiosulfate solution at 60 °C for three minutes, according to manufacturer's instructions (Millipore, AG105). MBP immunofluorescence staining was performed on brain slides using the following antibody combination: a primary chicken anti-MBP antibody (Millipore, AB9348; 1:200 dilution) with a secondary rabbit anti-chicken Cy3 antibody (Jackson, 303-166-003, 1:1000 dilution). Glial fibrillary acidic protein (GFAP) immunofluorescence was used to evaluate the degree of astrogliosis using: a primary rabbit anti-GFAP (Dako, Z0334, 1:500 dilution) with a secondary goat anti-rabbit FITC (Jackson,111-096-144,1:1000 dilution).

Fluorescence and bright field image acquisitions were performed using a conventional widefield system designed for epifluorescent and bright field imaging (Nikon Ti Microscope) equipped with Nikon DS-Qi2 monochrome and DS-Ri2 color cameras. The NIS-Elements 5.02 (Build 1266) software was used for wide field image acquisition. Quantitative analyses of immunofluorescence images were performed using NIH ImageJ analysis software (v1.51n). The levels of MBP and GFAP were determined based on the image-covering staining and expressed as percentage of the total area, as previously described (Guglielmetti et al., 2016a, 2016b, 2017b).

2.5. Statistical analyses

Results are expressed as mean ± standard deviation (SD). Statistical analyses of UTE-MTR, STE-MTR and MBP of the control mouse brain were performed using a One-Way ANOVA. A repeated measures ANOVA was used to evaluate statistical significance of the UTE-MTR and STE-MTR following CPZ diet. A One-Way ANOVA was used to assess statistical significance of the MBP and GFAP stainings following CPZ administration. The correlation between MR parameters and myelin content (MBP) or gliosis (GFAP) was assessed using linear regression. All given p-values obtained from One-Way ANOVA and repeated measures ANOVA were corrected for multiple testing using the Tukey HSD post-hoc test (*$p \leq 0.05$, **$p \leq 0.01$, ***$p \leq 0.001$, ****$p \leq 0.0001$).

3. Results

3.1. UTE-MTR and STE-MTR of the control mouse brain

We first evaluated the potential of UTE-MTR and STE-MTR to generate MR contrast of cerebral substructures in the control mouse brain at 7 T. As shown in Fig. 1A, white matter tract regions were visible as bright, hyper-intense MR signals on both UTE-MTR maps ($TE_1 = 76$ μs) and STE-MTR maps ($TE_2 = 3000$ μs). In contrast, ventricles and dorsal hippocampus appeared as regions of hypointense MR signal. ROIs from brain regions of various myelin content and arrangement were selected for subsequent analysis of MRI data within the white matter tracts, subcortical areas, and cortical areas (Fig. 1B).

In white matter tracks, UTE-MTR values from the internal capsule were significantly higher than values from the genu and the splenium (Fig. 1C, $p = 0.0002$ and $p < 0.0001$, respectively), while STE-MTR only detected a significant difference between the splenium and the internal capsule (Fig. 1D, $p = 0.0089$). Quantification of immunofluorescence images revealed a denser myelin content in the internal capsule compared to the splenium and genu (Fig. 1E and 1F, $p \leq 0.0269$).

In subcortical areas, UTE-MTR and STE-MTR from the thalamus and caudate/putamen were significantly higher than in the hippocampus (Fig. 1C, $p < 0.0001$ and $p < 0.0001$, respectively for UTE-MTR, and Fig. 1D, $p = 0.0008$ and $p = 0.0002$, respectively for STE-MTR). However, only UTE-MTR was able to differentiate between the caudate/putamen and the thalamus (Fig. 1C, $p < 0.0001$). MBP quantification revealed higher myelin load in the thalamus and caudate/putamen compared to hippocampus (Fig. 1F, $p < 0.0001$ and $p = 0.0168$, respectively), and between thalamus and caudate/putamen ($p < 0.0001$).

In cortical areas, only UTE-MTR was able to detect significant differences between the ROIs. UTE-MTR of the retro spinal cortex were higher than those of motor and somatosensory cortices (Fig. 1C, $p = 0.0089$ and $p = 0.0065$, respectively), in line with higher myelin content in the retro spinal cortex region compared to motor and somatosensory cortices (Fig. 1F, $p = 0.0139$ and $p = 0.0082$, respectively).

Last, we found a strong positive correlation between UTE-MTR and MBP (Fig. 1. G, $r^2 = 0.76$, $p < 0.0001$) as well as between STE-MTR and MBP (Fig. 1. H, $r^2 = 0.46$, $p < 0.0001$).

3.2. UTE-MTR and STE-MTR following CPZ-induced demyelination, remyelination and reactive gliosis

In this study, demyelination was achieved through the administration of 0.2% CPZ diet for a period of six weeks. Mice underwent longitudinal MRI exams prior to CPZ diet (W0), at W4 and W6 CPZ diet and after six week of recovery (W6 CPZ + W6 recovery). Histological analyses were performed at each corresponding MRI timepoints (Fig. 2A).

Representative UTE-MTR and STE-MTR maps, displayed as greyscale, clearly showed the hypointense splenium of the corpus callosum at W4 CPZ compared to W0, and its increased contrast back to hyperintense at W6 CPZ and W6 CPZ + W6 recovery. Additionally, decrease of UTE-MTR

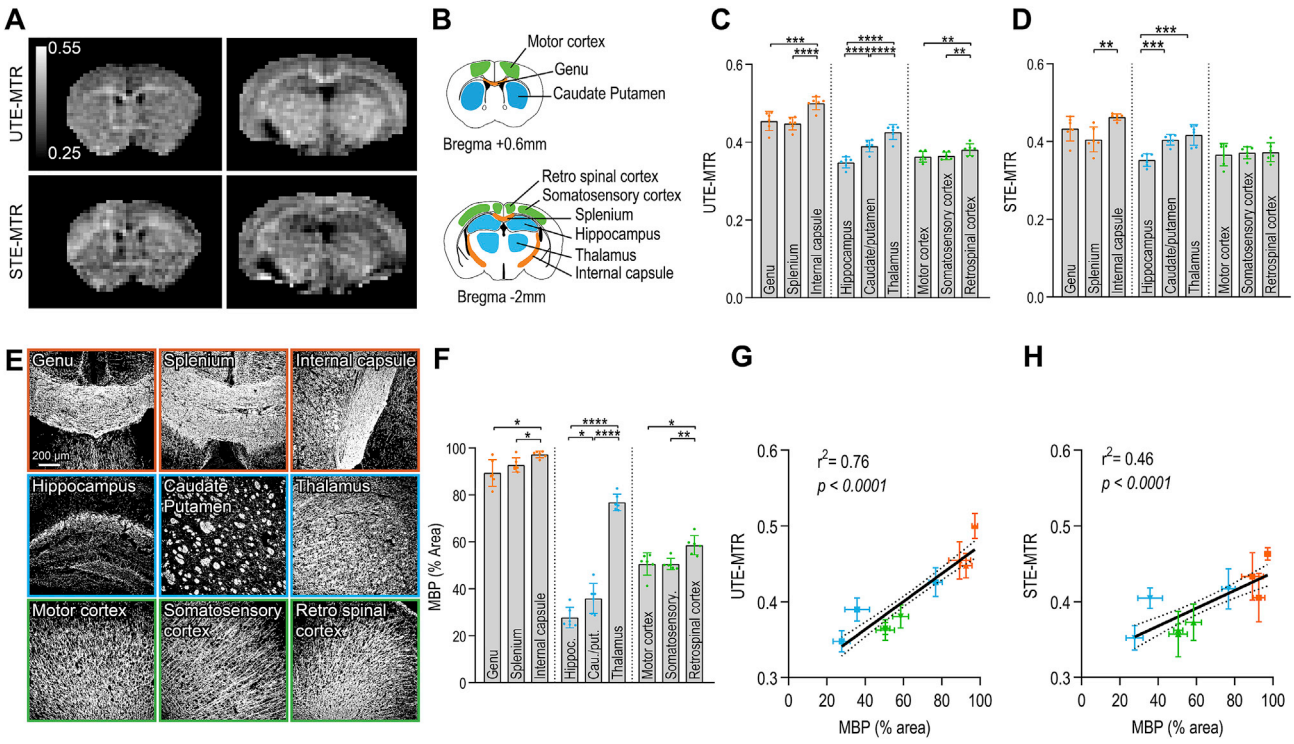

Fig. 1. UTE-MTR, STE-MTR and myelin immunofluorescence of the control mouse brain. **(A)** Representative UTE-MTR and STE-MTR maps (grey scale) obtained from a control (W0) mouse brain. The white matter tracts appeared as hyper-intense structures, while the ventricles appeared as hypo-intense regions. **(B)** Schematic representation of ROIs delineations of the white matter tracts (orange), subcortical grey matter (blue) and cortical grey matter (green) areas. **(C)** UTE-MTR and **(D)** STE-MTR values from all ROIs. **(E)** Representative MBP immunofluorescence images from a control mouse brain, demonstrating the heterogeneity in myelin load, compaction and arrangement between the selected ROIs (Scale bar = 200 µm). **(F)** Corresponding percent coverage of MBP staining. Correlations between **(G)** UTE-MTR and MBP, and **(H)** STE-MTR and MBP for all the ROIs, demonstrating a higher coefficient of correlation between UTE-MTR and MBP ($r^2 = 0.76$, $p < 0.0001$) compared to STE-MTR and MBP ($r^2 = 0.46$, $p < 0.0001$). Dark line shows the best-fit straight line from the linear regression analysis ±95% confidence intervals. Abbreviations: Hippoc.: Hippocampus, Cau./put.: Caudate/putamen, Somatosensory.: Somatosensory cortex. All values are reported as mean ± SD. One-Way ANOVA, Tukey HSD post hoc test, *$p \leq 0.05$, **$p \leq 0.01$, and ***$p \leq 0.001$, ****$p \leq 0.0001$ ($n = 6$ mice per group).

can be visually observed in the thalamic area following CPZ diet (Fig. 2B).

At W0, myelin appears as a red-purple coloration when stained with Black-Gold II, or as a dark grey-black contrast when stained for MBP (Fig. 2C). Both Black-Gold II and MBP staining confirmed demyelination of the splenium of the corpus callosum at W4 CPZ and widespread demyelination of the cortical and subcortical areas at W6 CPZ. At the end of the recovery period, remyelination was observed as Black-Gold II and MBP coloration displayed more intense staining.

Demyelination is often accompanied by neuro-inflammatory processes and reactive gliosis. As shown in Fig. 2D, astrogliosis, depicted by an increase of dark grey-black contrast from GFAP staining, occurred in the entire brain following W4 and W6 CPZ diet, and was particularly noticeable in the splenium, internal capsule, thalamus and cerebral cortex. At the end of the recovery period, astrogliosis was strongly reduced but persisted in the splenium.

UTE-MTR, STE-MTR, percent MBP and GFAP coverage were calculated for each ROIs defined in Fig. 1B and Supplementary Fig. 2. Results are presented in the three following subsections. Percent changes relative to Baseline and all p-values are shown in Supplementary Tables 1–4.

3.2.1. White matter tracts

The splenium of the corpus callosum showed the strongest decrease of UTE-MTR values at W4 CPZ, followed by a subsequent increase at W6 CPZ and W6 CPZ + W6 recovery (Fig. 3A). Similar changes were observed with STE-MTR, although just reaching significance level (Fig. 3B). MBP immunostaining of the splenium mirrored the changes detected with UTE-MTR and STE-MTR. Severe demyelination was observed at W4 CPZ, followed by remyelination at W6 CPZ and W6 CPZ + W6 recovery (Fig. 3C and Supplementary Fig. 3A, top row). Interestingly, astrogliosis was noted at W4 but reached its maximum at W6 CPZ. After recovery, astrocyte levels were decreased compared to W6 CPZ, but persistent astrogliosis was observed (Fig. 3D and Supplementary Fig. 4A, top row).

In the genu of the corpus callosum, UTE-MTR was decreased at W4 CPZ and W6 CPZ, and increased at the end of the recovery period (Fig. 3E). In contrast, STE-MTR was only decreased at W6 CPZ (Fig. 3F). Demyelination and astrogliosis were observed at W4 and W6 CPZ. At W6 CPZ + W6 recovery remyelination had occurred, however astrocyte levels remained significantly higher compared to W0 (Fig. 3G and Fig. 3H; Supplementary Fig. 3A and Supplementary Fig. 4A, middle rows).

In the internal capsule, UTE-MTR was significantly decreased only at W6 CPZ (Fig. 3I), and no differences in STE-MTR values were observed (Fig. 3J). Demyelination and astrogliosis were observed at W6 CPZ, followed by remyelination at W6 CPZ + W6 recovery (Fig. 3K and Fig. 3L; Supplementary Fig. 3A and Supplementary Fig. 4A, bottom rows).

3.2.2. Subcortical areas

In the thalamic area, UTE-MTR were lower following CPZ diet, (Fig. 4A), at W4 CPZ, W6 CPZ and W6 CPZ + W6 recovery. In contrast, STE-MTR values remained unchanged (Fig. 4B). MBP immunostaining was decreased, and astrogliosis was observed at W4 CPZ, W6 CPZ and after recovery (Fig. 4C and 4D;Supplementary Fig. 3 B, and Supplementary Fig. 4B, top rows).

In the caudate/putamen, UTE-MTR was decreased at W4 CPZ, W6 CPZ and W6 CPZ + W6 recovery (Fig. 4E), while STE-MTR was significantly decreased only at W4 and W6 CPZ (Fig. 4F). Demyelination and

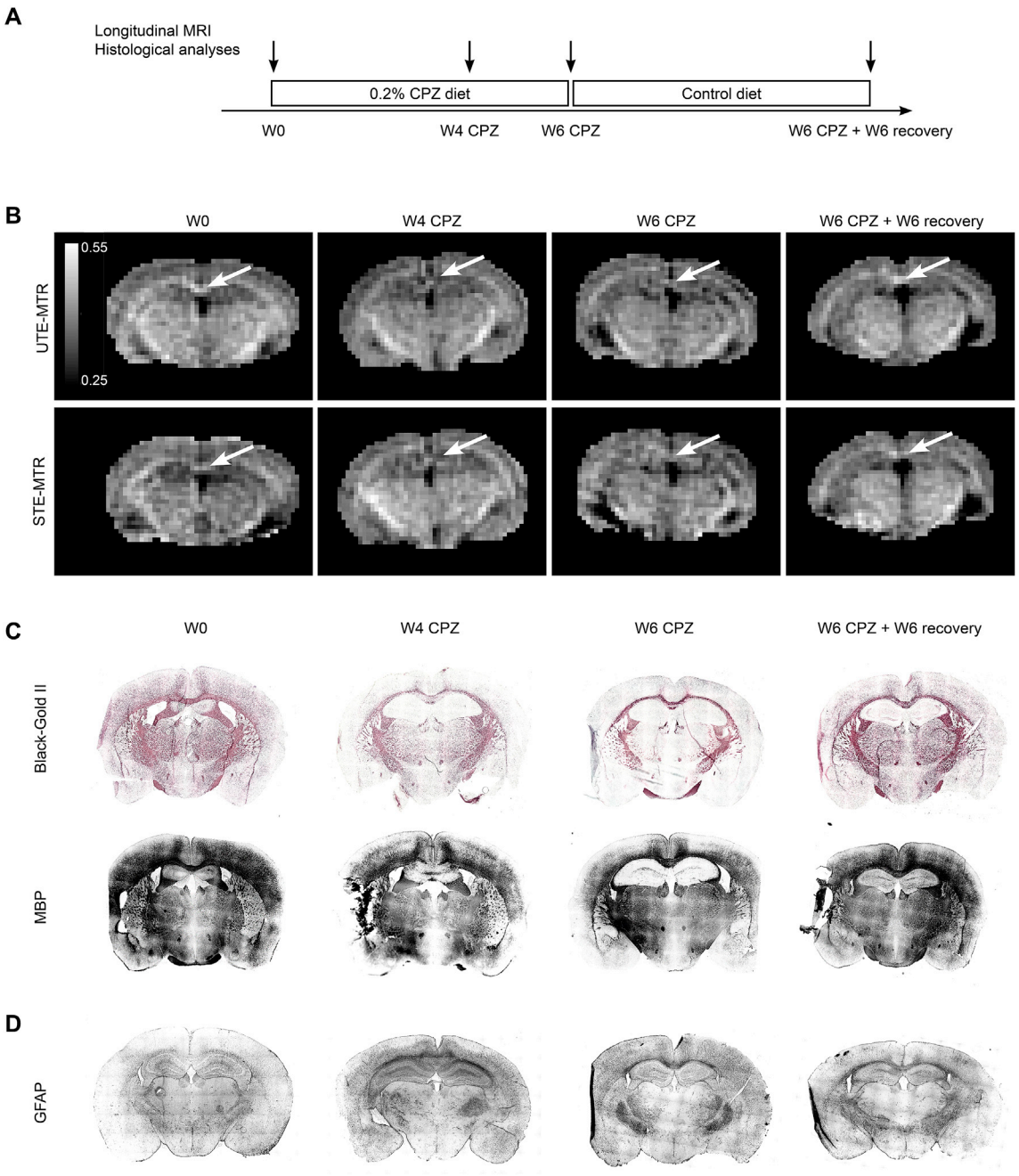

Fig. 2. Longitudinal UTE-MTR, STE-MTR and histological characterization of the CPZ mouse brain: representative datasets. **(A)** Experimental outline of the study indicating the time points of MRI and histological analyses, prior to CPZ diet (W0), after four (W4 CPZ) and six (W6 CPZ) weeks of CPZ diet, and after six weeks of recovery (W6 CPZ + W6 recovery). **(B)** Representative UTE-MTR maps and STE-MTR maps (grey scale) at all time points of interest. Decreased contrast can be seen on both UTE-MTR and STE-MTR maps for example in the splenium of the corpus callosum (white arrows) at W4 CPZ, followed by reappearance of contrast at W6 and W6 CPZ + W6 recovery. On the UTE-MTR maps, hypointensity can be observed in the thalamic area at W4 and W6 CPZ and W6 CPZ + W6 recovery. **(C)** Representative images of Black-Gold II and MBP staining demonstrated the spatial and temporal modulations in myelin levels, as seen by purple color or black contrast, respectively. Following CPZ diet, severe demyelination can be seen in the forebrain, as indicated by faint stainings for both Black-Gold II and MBP, particularly in the splenium at W4 CPZ, and thalamus and cortical areas at W6 CPZ. Reappearance of Black-Gold II and MBP staining can be observed at W6 CPZ + W6 recovery, demonstrating remyelination. (**D**) Representative GFAP immunofluorescence images showed important astrogliosis (GFAP, black contrast) in the splenium, internal capsule, thalamus and cortex following CPZ diet. At the end of the recovery period, astrogliosis was overall reduced but was still present in the splenium.

astrogliosis were observed at W4 CPZ, W6 CPZ and W6 CPZ + W6 recovery (Fig. 4G and Fig. 4H; Supplementary Fig. 3B and Supplementary Fig. 4B, middle rows).

In the hippocampus, UTE-MTR and STE-MTR could not detect any changes following CPZ diet (Fig. 4I-J). However, demyelination was detected after W4 CPZ and W6 CPZ. At the end of the recovery period, remyelination was observed (Fig. 4K and Supplementary Fig. 3B, bottom row). The hippocampus showed increased astrocyte immunostaining at W4 CPZ (Fig. 4L and Supplementary Fig. 4B, bottom row), which returned to control levels by W6 CPZ + W6 recovery.

3.2.3. *Cortical areas*

UTE-MTR of the retro spinal cortex was decreased at W4 CPZ, further decreased at W6 CPZ and remained significantly lower at the end of the

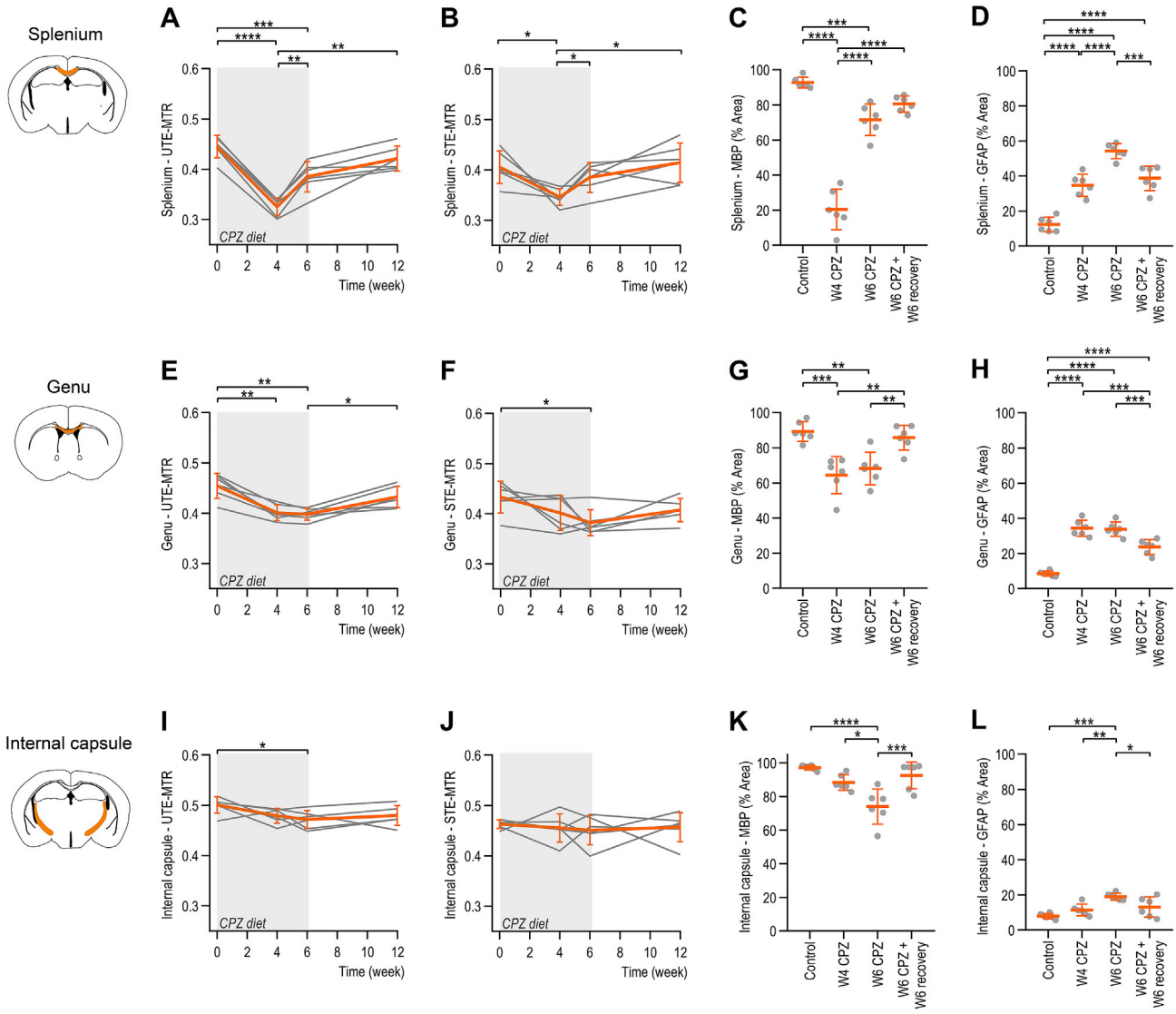

Fig. 3. Longitudinal UTE-MTR, STE-MTR, MBP and GFAP immunofluorescence of white matter tracts following CPZ diet. **(A)** UTE-MTR and **(B)** STE-MTR values were significantly decreased in the splenium after W4 CPZ, when **(C)** MBP staining indicated maximum demyelination. UTE-MTR and STE-MTR values from the splenium were increased at W6 CPZ and at W6 CPZ + W6 recovery, mirroring the MBP immunostaining outcome which indicated remyelination. **(D)** Astrogliosis was observed at W4 and W6 CPZ and remained after recovery. **(E)** UTE-MTR values from the genu were reduced at W4 and W6 CPZ, while **(F)** STE-MTR was only decreased at W6 CPZ. At W6 CPZ + W6 recovery, both UTE-MTR and STE-MTR values rose back to W0 values. **(G)** Demyelination was observed at W4 and W6 CPZ, and remyelination occurred by the end of the recovery period. Similarly as for the splenium, **(H)** astrogliosis was present at W4 and W6 CPZ and remained after recovery. **(I)** UTE-MTR values in the internal capsule were significantly decreased only at W6 CPZ while **(J)** STE-MTR did not detect any changes. **(K)** Demyelination and **(L)** astrocyte levels reached their maximum at W6 CPZ. All values are reported as mean ± SD. The grey lines represent mean value from each mouse and the colored lines represent mean ± SD of mean values from the individual subjects. One-Way ANOVA or repeated measures ANOVA, Tukey HSD post hoc test, *$p \leq 0.05$, **$p \leq 0.01$, and ***$p \leq 0.001$, ****$p \leq 0.0001$ (n = 6 mice).

recovery period (Fig. 5A). STE-MTR remained unchanged over the entire experimental period (Fig. 5B). MBP immunostaining mirrored the changes observed with UTE-MTR. Myelin level was decreased at W4 CPZ, followed by an additional decrease at W6 CPZ diet (Fig. 5C and Supplementary Fig. 3C, top row). While spontaneous remyelination occurred during the six weeks recovery period, myelin content remained significantly lower compared to control mice. Astrocytes levels significantly increased at W4 and W6 CPZ and returned to nearly control levels after recovery (Fig. 5L and Supplementary Fig. 4C, top row).

In somatosensory and motor cortices, UTE-MTR was significantly decreased only after W6 CPZ (Fig. 5E and Fig. 5I) and UTE-MTR of the somatosensory cortex remained lower at W6 CPZ + W6 recovery. STE-MTR did not detect any changes following CPZ diet (Fig. 5F and Fig. 5J). Demyelination and astrogliosis were observed in somatosensory and motor cortices at W4 and W6 CPZ. At the end of the recovery period, remyelination was incomplete but astrocyte levels returned to nearly control levels (Fig. 5G, Fig. 5H, Fig. 5K and Fig. 5L; Supplementary Fig. 3C and Supplementary Fig. 4C, middle and bottom rows).

3.3. Correlations between MR and immunohistological parameters

Potential associations between UTE-MTR/STE-MTR values and MBP/GFAP levels were explored using linear regression analyses (Fig. 6, Table 1 and Table 2). When considering all ROIs together, the strongest correlation was observed between UTE-MTR and MBP ($r^2 = 0.71$, $p < 0.0001$). Although lower, a significant correlation was also found between STE-MTR and MBP ($r^2 = 0.48$, $p < 0.0001$). No correlations between UTE-MTR and GFAP or STE-MTR and GFAP were observed.

When considering each ROI separately, we observed a significant correlation between UTE-MTR and MBP in the splenium, genu, internal

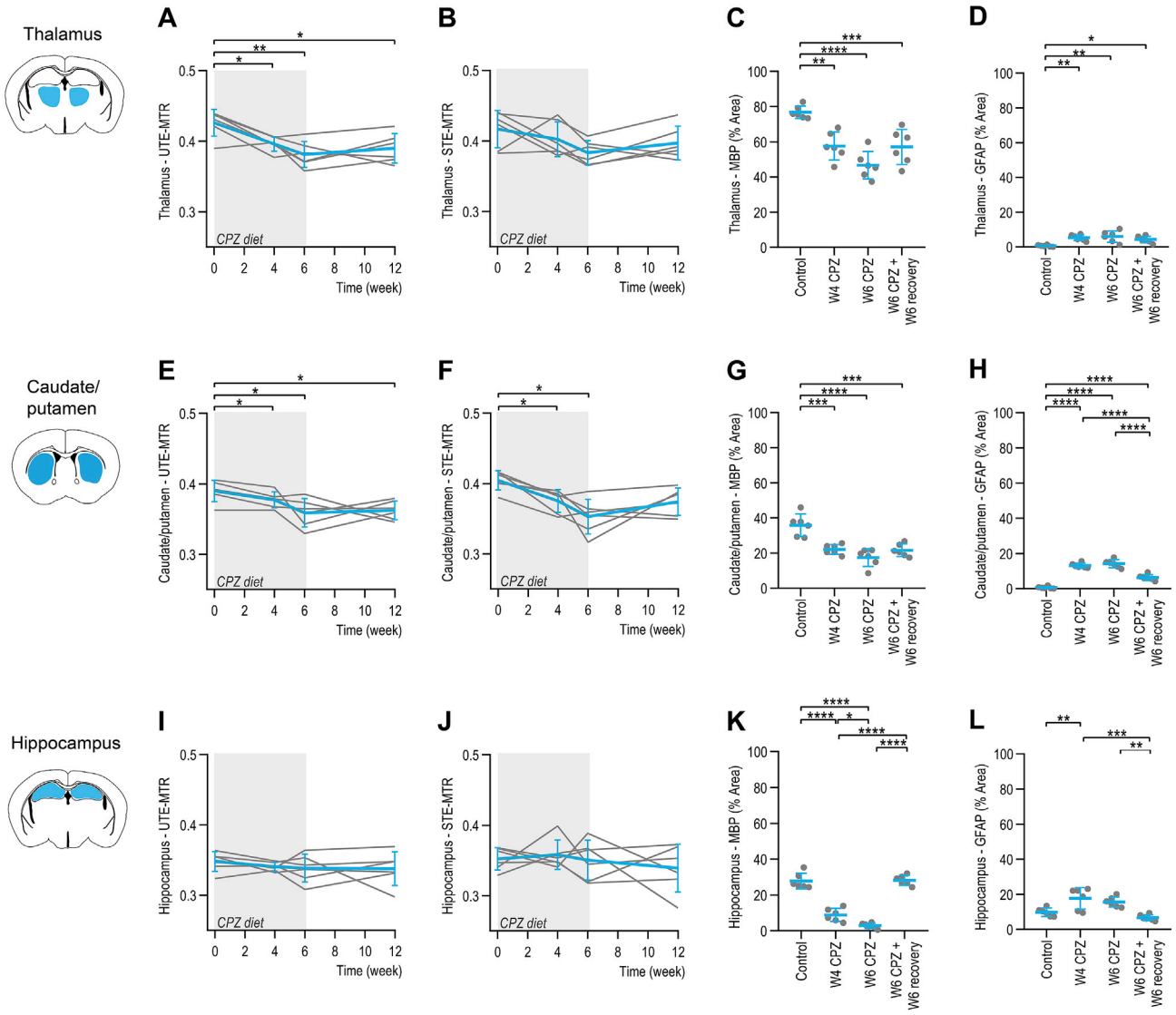

Fig. 4. Longitudinal UTE-MTR, STE-MTR and MBP and GFAP immunofluorescence of subcortical grey matter regions following CPZ diet. **(A)** UTE-MTR values of the thalamus were significantly decreased at W4 and W6 CPZ, and after recovery, while **(B)** STE-MTR remained unchanged. **(C)** MBP and **(D)** GFAP staining indicated demyelination at W4 and W6 CPZ and at W6 CPZ + W6 recovery. The strongest decrease of UTE-MTR corresponded to the maximal demyelination at W6 CPZ. **(E)** UTE-MTR values in the caudate/putamen were significantly decreased at W4 and W6 CPZ, and after recovery, while **(F)** STE-MTR was decreased only at W4 and W6 CPZ. **(G)** Demyelination and **(H)** astrogliosis were observed at every time point following CPZ diet, with astrogliosis reaching its highest level at W4 and W6 CPZ. **(I)** UTE-MTR and **(J)** STE-MTR of the hippocampus remained non significantly changed during the whole experimental period, despite significant **(K)** demyelination and **(L)** astrogliosis at W4 and W6 CPZ. All values are reported as mean ± SD. The grey lines represent mean value from each mouse and the colored lines represent mean ± SD of mean values from the individual subjects. One-Way ANOVA or repeated measures ANOVA, Tukey HSD post hoc test, *$p \leq 0.05$, **$p \leq 0.01$, and ***$p \leq 0.001$, ****$p \leq 0.0001$ ($n = 6$ mice).

capsule, thalamus, caudate/putamen, retro spinal, somatosensory and motor cortices (Table 1, Supplementary Fig. 5). Significant correlations were also found between UTE-MTR and GFAP in the splenium, genu, internal capsule, thalamus and caudate/putamen. No significant correlations were found between STE-MTR and GFAP in the cortical areas (Table 1, Supplementary Fig. 6).

As for STE-MTR values, we found significant correlations between STE-MTR and MBP in the splenium, genu, thalamus and caudate/putamen (Table 2, Supplementary Fig. 7). Significant correlation between STE-MTR and GFAP were found in the genu, thalamus and caudate/putamen (Table 2, Supplementary Fig. 8).

4. Discussion

In this study, 3D UTE-MT and STE-MT imaging sequences were implemented on a clinical 7 T scanner and used to obtain MR images of the mouse brain. We first demonstrated that STE-MTR and UTE-MTR maps enabled the visualization of anatomically distinct regions, including white matter tracts, subcortical grey matter areas and cortical grey matter areas in the normal mouse brain. We then showed that both STE-MTR and UTE-MTR measures could detect cerebral tissue alterations following the administration of the neurotoxic compound CPZ. Importantly, UTE-MTR values were more strongly correlated with myelin immunostaining than STE-MTR, in both white and grey matter regions. Furthermore, UTE-MTR showed significantly higher discrimination between brain regions than STE-MTR in the healthy mouse brain, and additionally enabled the detection of CPZ-induced alterations in multiple white and grey matter regions, including in the cerebral cortex.

Inflammatory demyelination and spontaneous remyelination were achieved by feeding mice a diet supplemented with 0.2% CPZ for a

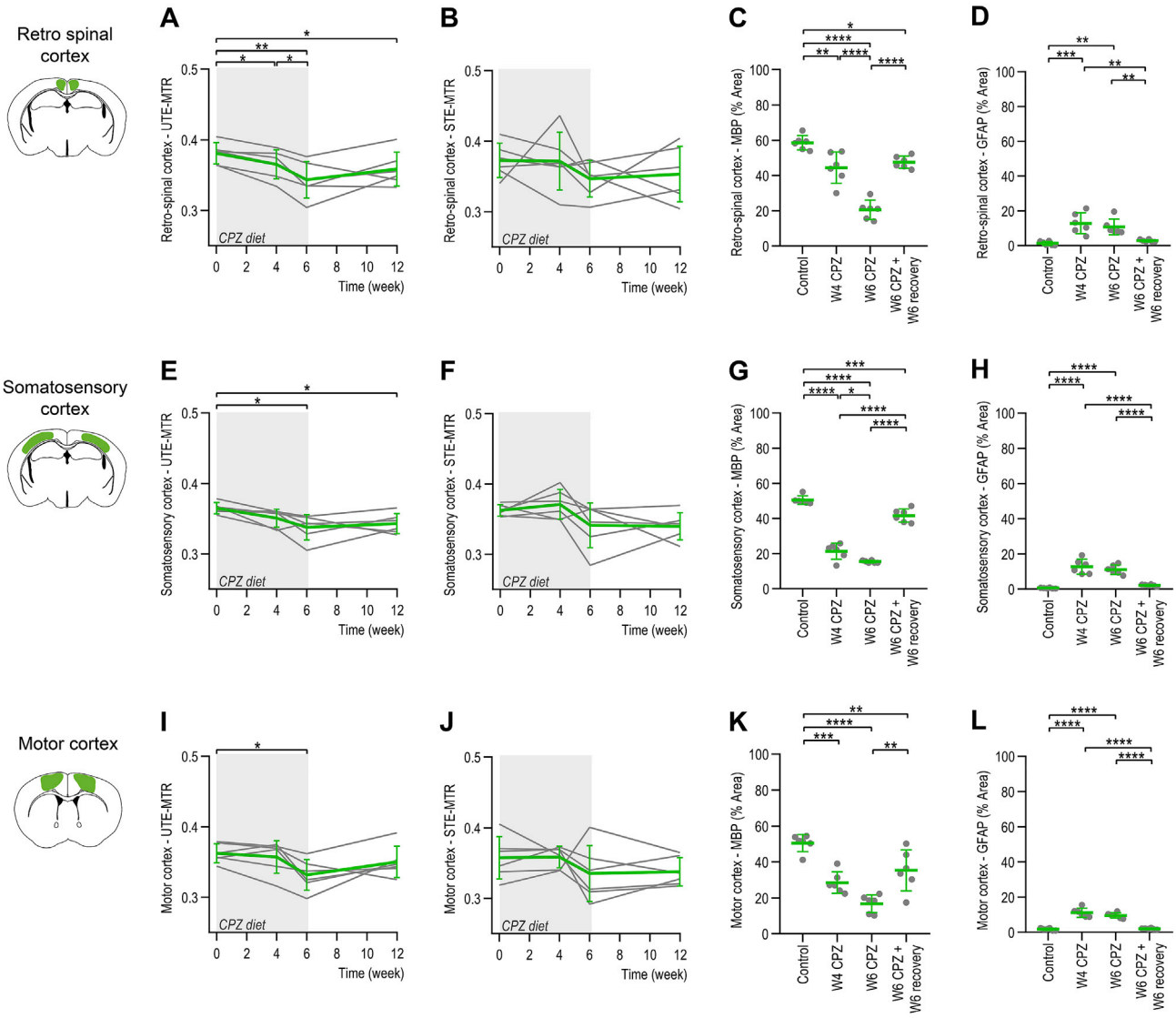

Fig. 5. Longitudinal UTE-MTR, STE-MTR and MBP and GFAP immunofluorescence of cortical grey matter regions following CPZ diet. **(A)** UTE-MTR values of the retro spinal cortex were significantly decreased at W4 and W6 CPZ, and after W6 CPZ + W6 recovery, while **(B)** STE-MTR remained unchanged. **(C)** MBP staining mirrored the UTE-MTR results, indicating demyelination at W4 and W6 CPZ and after recovery, with the strongest decrease of UTE-MTR corresponding to the maximal demyelination at W6 CPZ. **(D)** Astrogliosis was present at W4 and W6 CPZ. **(E)** UTE-MTR of the somatosensory cortex was decreased at W6 CPZ and after recovery, while **(F)** STE-MTR remained unchanged. **(G)** Demyelination was observed at W4, W6 CPZ and persisted after W6 CPZ + W6 recovery, while **(H)** astrogliosis was only observed at W4 and W6 CPZ. **(I)** UTE-MTR of the motor cortex was decreased at W6 CPZ and after recovery, while **(J)** STE-MTR remained unchanged. **(K)** Demyelination was observed at W4, W6 CPZ and after recovery. **(L)** Astrogliosis was present at W4 and W6 CPZ. All values are reported as mean ± SD. The grey lines represent mean value from each mouse and the colored lines represent mean ± SD of mean values from the individual subjects. One-Way ANOVA or repeated measures ANOVA, Tukey HSD post hoc test, *$p \leq 0.05$, **$p \leq 0.01$, and ***$p \leq 0.001$, ****$p \leq 0.0001$ ($n = 6$ mice).

period of six weeks, followed by a recovery period of six additional weeks. While the CPZ mouse model does not fully reflect the heterogeneity of lesions found in MS patients, CPZ-induced lesions have been shown to resemble pattern III and IV of MS lesions, with primary oligodendrocyte damage and demyelination, highlighting its clinical relevance (Lucchinetti et al., 2000; Reich et al., 2018; Torkildsen et al., 2008). Furthermore and importantly, the CPZ model presents many advantages over other demyelinating models, in particular a well-defined pathology in time, a high reproducibility in the location of lesions in the brain, and an extensive histological characterization (Goldberg et al., 2015; Gudi et al., 2009; Praet et al., 2014). Such features make this model highly suitable for validation of the proposed imaging techniques while requiring low number of animals (Fjaer et al., 2013; Guglielmetti et al., 2016b, 2017b; Jelescu et al., 2016; Khodanovich et al., 2017; Petiet et al., 2016).

In this study, differences between UTE-MTR and STE-MTR are expected to be due to two main biophysical-related phenomena: (1) the potential of UTE to directly capture signals from bound protons in the myelin phospholipid membranes (Horch et al., 2011; Wilhelm et al., 2012) as well as (2) increased sensitivity of UTE to myelin water protons that may experience MT saturation. Other expected sources of signal (intra and extra cellular water) have much longer T_2^* ~ 30 ms at 7 T (van Gelderen et al., 2012), and thus should be approximately equivalent for UTE- and STE-MTR and not induce major differences.

For (1) the bound protons, we have measured a T_2^* of ≈0.2 ms *in vivo* at 7 T (Boucneau et al., 2018). This relaxation time is notably shorter than our readout time of 1320 μs, and thus the detection of this bound pool using our sequence is limited. For (2) myelin water, previous studies have reported a T_2^* of ~6 ms at 7 T (van Gelderen et al., 2012). STE should thus have less myelin water signal, approximately $\exp(-TE/T^2*)$

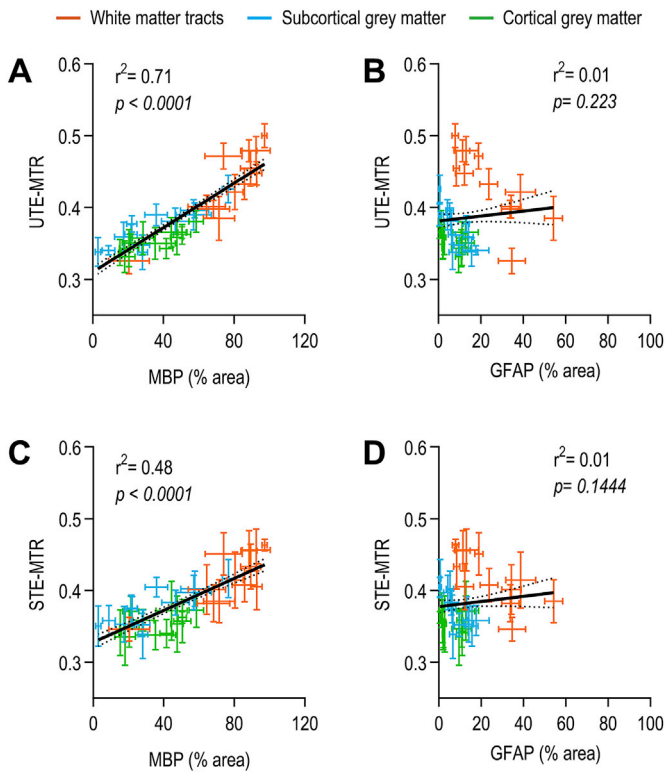

Fig. 6. Correlations between UTE-MTR/STE-MTR values and MBP/GFAP immunofluorescence levels for all ROIs at all time points of CPZ diet. Correlations between (A) UTE-MTR and myelin content (MBP), (B) UTE-MTR and astrocyte levels (GFAP), (C) STE-MTR and MBP and (D) STE-MTR and GFAP for all time points combined and all the ROIs: white matter tracts (orange), subcortical (blue) and cortical (green) grey matter areas. All values are reported as mean ± SD. Dark lines show the best-fit linear regression analysis ±95% confidence intervals.

= exp(-3 ms/6 ms) ~ 0.6, or 60% of the myelin water signal compared to the UTE acquisition. Based on these T^2* measurements and our TE values, we speculate the main difference between UTE- and STE-MTR is due to myelin water that is experiencing magnetization transfer.

Other potential differences between UTE- and STE-MTR values might be due to differences in signal-to-noise ratio (SNR) and/or variance of the images. UTE images displayed a higher SNR than STE images (Supplementary Fig. 9B, p = 0.0021 and p = 0.0077 for unsaturated and saturated images, respectively). However, as the SNR in the brain ROIs when averaging across voxels is very high for both UTE and STE images (>100), the noise effect is much smaller than the differences observed between UTE and STE. Furthermore, we found no significant differences between the variance of UTE-MTR and STE-MTR (Supplementary Fig. 9C, p = 0.1295). Therefore, the differences we observed between UTE- and STE-MTR are unlikely due to noise or variance effects.

The results we obtained with STE-MTR are in full agreement with a longitudinal study by Fjaer et al. (2013), in which MTR was performed on a preclinical 7 T system. In that study, MTR values were significantly decreased in the corpus callosum and the caudate/putamen following CPZ administration in mice, but no changes were detected in cortical areas. A few other studies focusing on the corpus callosum of CPZ-treated mice have associated MTR values to oligodendrocytes numbers and myelin (Boretius et al., 2012; Guglielmetti et al., 2016a; Merkler et al., 2005; Thiessen et al., 2013; Turati et al., 2015), and to markers of gliosis (Guglielmetti et al., 2016a; Zaaraoui et al., 2008).

In line with these observations, we also showed that both UTE- and STE-MTR values correlate with myelin content as measured by MBP immunostaining in healthy control mice. Interestingly, these correlations between UTE-MTR or STE-MTR and MBP immunostaining were also observed during toxic-induced demyelination following CPZ diet (Tables 1 and 2), demonstrating that modulations in both UTE- and STE-MTR values were associated with longitudinal changes in myelin content. However, it is important to note that demyelination is often accompanied by changes in the brain microenvironment, such as immune response, reactive gliosis, neurodegeneration and/or edema (Gudi et al., 2009; Lucchinetti et al., 2011; Praet et al., 2014; Reich et al., 2018). In particular, gliosis and swelling of astrocyte processes, as indicated by an increase of GFAP immunostaining, may contribute to an increase of non-myelin associated water and thus might influence the measured UTE-MTR and STE-MTR values (Guglielmetti et al., 2016a; Zaaraoui et al., 2008). In this study, although GFAP staining was increased following CPZ administration, we did not find any correlations between UTE-MTR or STE-MTR values and GFAP immunostaining (Tables 1 and 2). However, it is still difficult to completely disentangle demyelination and gliosis as these processes mostly occur concomitantly (Supplementary Table 5). Consequently, when we performed correlations on individual ROIs, we observed a strong positive correlation of UTE-MTR and STE-MTR with MBP and an inverse correlation with GFAP. In this analysis, two areas are of particular interest: (1) the splenium, which displays a distinct temporal pattern of demyelination and astrogliosis (Fig. 3, maximal demyelination at W4 CPZ and maximal astrogliosis at W6 CPZ), showed that UTE-MTR was more significantly correlated to MBP than GFAP, and that STE-MTR was solely significantly correlated with MBP; (2) the cortical grey matter ROIs show strong correlation between MBP and GFAP immunostaining (Supplementary Table 5) but only UTE-MTR was able to detect association with MBP at the ROIs level (Table 1), indicating that the strongest correlate of UTE-MTR was MBP immunostaining.

Cortical demyelination has been linked with disease progression and

Table 1
UTE-MTR and MBP, and UTE-MTR and GFAP correlation parameters.

Region of interest	MBP			GFAP		
	Linear regression equation	r^2	*p-value*	Linear regression equation	r^2	*p-value*
All	Y = 0.0016*X + 0.31	0.71	***<0.0001*** (****)	Y = 0.0003*X + 0.38	0.01	*0.2231*
White Matter Tracts						
Splenium	Y = 0.0016*X + 0.29	0.78	***<0.0001*** (****)	Y = −0.0014*X + 0.44	0.18	***0.0410*** (*)
Genu	Y = 0.0021*X + 0.26	0.59	***<0.0001*** (****)	Y = −0.0022*X + 0.48	0.61	***<0.0001*** (****)
Internal capsule	Y = 0.0010*X + 0.39	0.21	***0.0257*** (*)	Y = −0.0024*X + 0.51	0.24	***0.0150*** (*)
Subcortical Grey Matter						
Thalamus	Y = 0.0015*X + 0.31	0.51	***0.0001*** (***)	Y = −0.0078*X + 0.43	0.47	***0.0002*** (***)
Caudate/Putamen	Y = 0.0016*X + 0.33	0.35	***0.0021*** (***)	Y = −0.0014*X + 0.38	0.17	***0.0453*** (*)
Hippocampus	Y = 0.0002*X + 0.34	0.01	*0.6140*	Y = −0.0001*X + 0.34	0.00	*0.8598*
Cortical Grey Matter						
Retro spinal cortex	Y = 0.0009*X + 0.32	0.28	***0.0085*** (**)	Y = −0.0015*X + 0.37	0.09	*0.1553*
Somatosensory cortex	Y = 0.0005*X + 0.33	0.19	***0.0322*** (*)	Y = −0.0010*X + 0.36	0.10	*0.1302*
Motor cortex	Y = 0.0008*X + 0.32	0.19	***0.0309*** (*)	Y = −0.0011*X + 0.36	0.05	*0.3092*

Parameters from regression analysis between UTE-MTR and myelin content (MBP) or astrogliosis (GFAP).

Table 2
MTR and MBP, and MTR and GFAP correlation parameters.

Region of interest	MBP			GFAP		
	Linear regression equation	r^2	*p-value*	Linear regression equation	r^2	*p-value*
AllD	Y = 0.0011*X + 0.33	0.48	***<0.0001*** (****)	Y = 0.0004*X + 0.38	0.01	*0.1444*
White Matter Tracts						
Splenium	Y = 0.0009*X + 0.33	0.42	***0.0006*** (***)	Y = −0.0004*X + 0.40	0.02	*0.4851*
Genu	Y = 0.0013*X + 0.30	0.20	***0.0300*** (*)	Y = −0.0016*X + 0.45	0.30	***0.0090*** (**)
Internal capsule	Y = 0.0005*X + 0.42	0.03	*0.4252*	Y = −0.0010*X + 0.47	0.03	*0.4181*
Subcortical Grey Matter						
Thalamus	Y = 0.0011*X + 0.34	0.23	***0.0186*** (*)	Y = −0.0051*X + 0.42	0.19	***0.0355*** (*)
Caudate/Putamen	Y = 0.0026*X + 0.31	0.50	***0.0001*** (***)	Y = −0.0030*X + 0.40	0.41	***0.0007*** (***)
Hippocampus	Y = −0.0003*X + 0.36	0.02	*0.4715*	Y = 0.0013*X + 0.33	0.05	*0.2738*
Cortical Grey Matter						
Retro spinal cortex	Y = 0.0006*X + 0.33	0.07	*0.2047*	Y = −0.0003*X + 0.36	0.00	*0.8511*
Somatosensory cortex	Y = 0.0001*X + 0.35	0.00	*0.8713*	Y = 0.0005*X + 0.35	0.01	*0.5886*
Motor cortex	Y = 0.0005*X + 0.33	0.05	*0.3065*	Y = 0.0001*X + 0.35	0.00	*0.9254*

Parameters from regression analysis between MTR and myelin content (MBP) or astrogliosis (GFAP).

cognitive impairment in MS, but remains invisible using conventional MRI (Kutzelnigg and Lassmann, 2006; Kutzelnigg et al., 2005; Lucchinetti et al., 2011; Stadelmann et al., 2008). Therefore, there is an urgent need to develop new imaging methods that would enable the detection and longitudinal follow up of cortical alterations. The cortex of CPZ-fed mice undergoes severe demyelination upon a few weeks of CPZ administration, as confirmed by post-mortem histological analyses (Gudi et al., 2009; Guglielmetti et al., 2016b; Hibbits et al., 2009; Skripuletz et al., 2008); however only a few MR imaging studies have been able to detect cortical changes in this model *in vivo*. Specifically, diffusion kurtosis imaging (Guglielmetti et al., 2016b), and macromolecular proton fraction (MPF) imaging (Khodanovich et al., 2017) reported cortical changes following CPZ administration. In this study, we showed that UTE-MTR was significantly decreased in cortical areas and only correlated with myelin levels as measured by MBP immunostaining. It is important to note that while every cortical areas undergo remyelination once the CPZ diet is removed, complete remyelination is not reached by the end of the recovery period (Fig. 5, W6 CPZ + W6 recovery) and UTE-MTR remained significantly decreased. The observation of these long-lasting changes may be due to incomplete remyelination at the time of MR exams, or reflect neurodegeneration and subsequent lower number of axonal projections that can be remyelinated. It is also possible that changes to the extra cellular matrix after remyelination and tissue remodeling play a role in the observed decreased UTE-MTR values at the end of the recovery period.

The hippocampal formation is an important region of the mouse brain due to its crucial role in cognitive processes and memory formation. The dorsal hippocampal formation undergo severe demyelination upon CPZ administration (Koutsoudaki et al., 2009; Norkute et al., 2009), followed by spontaneous remyelination once CPZ is removed. Unfortunately, neither UTE-MTR or STE-MTR were able to detect changes at any time points, which could be explained by the particular myelin arrangement in this structure, with low myelin content overall except for the densely myelinated stratum lacunosum molecular region (Fig. 1E-F). Another possibility is that the spatial resolution achieved in this study (200 × 200 × 500 μm^3) is on the rather low side for mouse brain imaging (due to clinical hardware use), and therefore partial volume effect from the ventricles or from voxels containing both white and grey matter might influence our outcome, particularly for this specific ROI of complex myelin arrangement. Partial volume effect may also affect our findings from white matter tracts, which show a thickness of 250–500 μm in coronal section according to Paxinos mouse atlas, but much less for the other ROIs within cortical and subcortical areas that cover larger brain regions. To minimize this effect we carefully delineated small ROIs over several consecutives MR slices, as indicated in Supplementary Fig. 2. It should be noted that the resolution used in this study is comparable to other studies performed in the cuprizone model using diffusion kurtosis imaging and investigating changes in white matter tracts and grey matter regions (Falangola et al., 2014; Guglielmetti et al., 2016b). Last, our goal is the clinical translation of the proposed sequences on the clinical 7 T for future patient's studies (Wei et al., 2018). While this comes with limited spatial resolution due to clinical hardware setting, it still remains of utmost importance to evaluate the association of UTE-MTR and STE-MTR values to histological markers in a very reproducible animal model, as such approach is not possible in clinical studies.

In this study, we used MT imaging to generate MR images with pool-selective contrast and opted for an offset frequency of −1800 Hz based on a prior study that investigated a range of offset frequencies (−1200 Hz to −3000 Hz) and showed adequate grey/white matter contrast at an offset frequency of −1800 Hz (Wei et al., 2018). Alternative methods to generate MR images with pool-selective contrast include suppression of long-T_2 components by subtracting two echoes with different echo times (Du et al., 2009), by using specially designed long-T_2 suppression RF pulses (Larson et al., 2006), by applying an inversion recovery UTE acquisition scheme (Du et al., 2014; Piedzia et al., 2014), or, more recently, by appropriate water suppression through diffusion weighting (UTE-Diff) (Soustelle et al., 2019).

Quantitative MTR (qMT) enables the estimation of the bound protons fraction (f), a metric that has been shown to detect changes associated with myelin content in cortical areas, though only *ex vivo* in fixed mouse brains (Soustelle et al., 2019; Thiessen et al., 2013). However, post-processing of qMT may be challenging and other studies performed *in vivo* following CPZ administration have only reported changes in the corpus callosum (white matter) (Turati et al., 2015). Comparing our method to qMT and other myelin imaging methods would be interesting. However, such studies are beyond the scope of our paper.

Last, this study also highlights the feasibility of 3D UTE-MT imaging on a 7 T clinical scanner within scan times suitable for human studies. We were able to obtain high-resolution UTE-MTR maps using clinical gradients and a dedicated mouse brain surface coil in 40 min of scan time. This same sequence and system has also used for human imaging studies, achieving 1 × 1 × 3 mm^3 resolution and whole brain coverage for 3D UTE-MT in under 10 min (Wei et al., 2018). An advantage of UTE-MTR compared to conventional T_2 relaxometry, UTE T_2* relaxometry or IR sequences is the potential for shorter imaging times, as it relies on only two acquisitions. Furthermore, UTE-MTR is a quantitative metric that has remarkably improved MR contrast compared to MT imaging at conventional TEs.

5. Conclusions

We demonstrated that UTE-MTR and STE-MTR values correlated with myelin content in the control mouse brain and in a MS murine model. Both STE-MTR and UTE-MTR values were decreased following CPZ-induced brain alterations. UTE-MTR was able to detect changes in the highest number of regions (8 out of 9) compared to STE-MTR (3 out of 9),

and only UTE-MTR was able to detect alterations in the cortical areas. Comparing the methods in terms of their statistical sensitivity to lesions, UTE-MTR demonstrated the highest coefficients of correlation to myelin immunostaining, suggesting that UTE-MTR is more sensitive to MT saturation of the myelin water than STE-MTR.

Altogether, we showed that UTE-MT imaging can detect brain tissue alterations in white and grey matter regions in the healthy and CPZ mouse brain on a clinical 7 T MR system. Furthermore, our results show that UTE-MTR values correlate with changes in myelination levels, thus demonstrating the potential of UTE-MTR as a clinically translatable sequence that may improve characterization of damaged brain tissue in neurological disorders.

Author contributions

Caroline Guglielmetti: Conceptualization, Methodology, Formal analysis, Investigation, Writing - Original Draft, Writing - Review & Editing, Visualization.

Tanguy Boucneau: Methodology, Investigation, Writing - Review & Editing.

Peng Cao: Investigation.

Annemie Van der Linden: Resources, Supervision.

Peder E.Z. Larson: Conceptualization, Methodology, Formal analysis, Resources Writing - Review & Editing, Supervision, Funding acquisition.

Myriam M. Chaumeil: Conceptualization, Methodology, Formal analysis, Resources Writing - Original Draft, Writing - Review & Editing, Visualization, Supervision, Funding acquisition.

Acknowledgments

This work was supported by research grants: NIH R21NS089004, R01NS102156, NMSS research grants PP3360 and RG-1701-26630, fellowship from the NMSS (FG-1507-05297) and from the Flemish Institute for Science and Technology.

Appendix A. Supplementary data

Supplementary data to this article can be found online at https://doi.org/10.1016/j.neuroimage.2019.116415.

References

Baumann, N., Pham-Dinh, D., 2001. Biology of oligodendrocyte and myelin in the mammalian central nervous system. Physiol. Rev. 81, 871–927.

Boretius, S., Escher, A., Dallenga, T., Wrzos, C., Tammer, R., Bruck, W., Nessler, S., Frahm, J., Stadelmann, C., 2012. Assessment of lesion pathology in a new animal model of MS by multiparametric MRI and DTI. Neuroimage 59, 2678–2688.

Boucneau, T., Cao, P., Tang, S., Han, M., Xu, D., Henry, R.G., Larson, P.E.Z., 2018. In vivo characterization of brain ultrashort-T2 components. Magn. Reson. Med. 80, 726–735.

Carl, M., Ma, Y., Du, J., 2018. Theoretical analysis and optimization of ultrashort echo time (UTE) imaging contrast with off-resonance saturation. Magn. Reson. Imaging 50, 12–16.

Chang, E.Y., Bae, W.C., Shao, H., Biswas, R., Li, S., Chen, J., Patil, S., Healey, R., D'Lima, D.D., Chung, C.B., Du, J., 2015a. Ultrashort echo time magnetization transfer (UTE-MT) imaging of cortical bone. NMR Biomed. 28, 873–880.

Chang, E.Y., Du, J., Biswas, R., Statum, S., Pauli, C., Bae, W.C., Chung, C.B., 2015b. Off-resonance saturation ratio obtained with ultrashort echo time-magnetization transfer techniques is sensitive to changes in static tensile loading of tendons and degeneration. J. Magn. Reson. Imaging 42, 1064–1071.

Du, J., Ma, G., Li, S., Carl, M., Szeverenyi, N.M., VandenBerg, S., Corey-Bloom, J., Bydder, G.M., 2014. Ultrashort echo time (UTE) magnetic resonance imaging of the short T2 components in white matter of the brain using a clinical 3T scanner. Neuroimage 87, 32–41.

Du, J., Takahashi, A.M., Bydder, M., Chung, C.B., Bydder, G.M., 2009. Ultrashort TE imaging with off-resonance saturation contrast (UTE-OSC). Magn. Reson. Med. 62, 527–531.

Falangola, M.F., Guilfoyle, D.N., Tabesh, A., Hui, E.S., Nie, X., Jensen, J.H., Gerum, S.V., Hu, C., LaFrancois, J., Collins, H.R., Helpern, J.A., 2014. Histological correlation of diffusional kurtosis and white matter modeling metrics in cuprizone-induced corpus callosum demyelination. NMR Biomed. 27, 948–957.

Fan, S.J., Ma, Y., Chang, E.Y., Bydder, G.M., Du, J., 2017. Inversion recovery ultrashort echo time imaging of ultrashort T2 tissue components in ovine brain at 3 T: a sequential D2 O exchange study. NMR Biomed. 30.

Fan, S.J., Ma, Y., Zhu, Y., Searleman, A., Szeverenyi, N.M., Bydder, G.M., Du, J., 2018. Yet more evidence that myelin protons can be directly imaged with UTE sequences on a clinical 3T scanner: bicomponent T2* analysis of native and deuterated ovine brain specimens. Magn. Reson. Med. 80, 538–547.

Filippi, M., Rocca, M.A., 2011. MR imaging of multiple sclerosis. Radiology 259, 659–681.

Filippi, M., Rocca, M.A., Ciccarelli, O., De Stefano, N., Evangelou, N., Kappos, L., Rovira, A., Sastre-Garriga, J., Tintore, M., Frederiksen, J.L., Gasperini, C., Palace, J., Reich, D.S., Banwell, B., Montalban, X., Barkhof, F., Group, M.S., 2016. MRI criteria for the diagnosis of multiple sclerosis: MAGNIMS consensus guidelines. Lancet Neurol. 15, 292–303.

Fjaer, S., Bo, L., Lundervold, A., Myhr, K.M., Pavlin, T., Torkildsen, O., Wergeland, S., 2013. Deep gray matter demyelination detected by magnetization transfer ratio in the cuprizone model. PLoS One 8, e84162.

Goldberg, J., Clarner, T., Beyer, C., Kipp, M., 2015. Anatomical distribution of cuprizone-induced lesions in C57BL6 mice. J. Mol. Neurosci. 57, 166–175.

Green, A.J., Gelfand, J.M., Cree, B.A., Bevan, C., Boscardin, W.J., Mei, F., Inman, J., Arnow, S., Devereux, M., Abounasr, A., Nobuta, H., Zhu, A., Friessen, M., Gerona, R., von Budingen, H.C., Henry, R.G., Hauser, S.L., Chan, J.R., 2017. Clemastine fumarate as a remyelinating therapy for multiple sclerosis (ReBUILD): a randomised, controlled, double-blind, crossover trial. Lancet 390, 2481–2489.

Groebe, A., Clarner, T., Baumgartner, W., Dang, J., Beyer, C., Kipp, M., 2009. Cuprizone treatment induces distinct demyelination, astrocytosis, and microglia cell invasion or proliferation in the mouse cerebellum. Cerebellum 8, 163–174.

Grosse, U., Syha, R., Martirosian, P., Wuerslin, C., Horger, M., Grozinger, G., Schick, F., Springer, F., 2013. Ultrashort echo time MR imaging with off-resonance saturation for characterization of pathologically altered Achilles tendons at 3 T. Magn. Reson. Med. 70, 184–192.

Gudi, V., Moharregh-Khiabani, D., Skripuletz, T., Koutsoudaki, P.N., Kotsiari, A., Skuljec, J., Trebst, C., Stangel, M., 2009. Regional differences between grey and white matter in cuprizone induced demyelination. Brain Res. 1283, 127–138.

Guglielmetti, C., Le Blon, D., Santermans, E., Salas-Perdomo, A., Daans, J., De Vocht, N., Shah, D., Hoornaert, C., Praet, J., Peerlings, J., Kara, F., Bigot, C., Mai, Z., Goossens, H., Hens, N., Hendrix, S., Verhoye, M., Planas, A.M., Berneman, Z., van der Linden, A., Ponsaerts, P., 2016a. Interleukin-13 immune gene therapy prevents CNS inflammation and demyelination via alternative activation of microglia and macrophages. Glia 64, 2181–2200.

Guglielmetti, C., Najac, C., Didonna, A., Van der Linden, A., Ronen, S.M., Chaumeil, M.M., 2017a. Hyperpolarized 13C MR metabolic imaging can detect neuroinflammation in vivo in a multiple sclerosis murine model. Proc. Natl. Acad. Sci. U. S. A. 114, E6982–E6991.

Guglielmetti, C., Najac, C., Didonna, A., Van der Linden, A., Ronen, S.M., Chaumeil, M.M., 2017b. Hyperpolarized (13)C MR metabolic imaging can detect neuroinflammation in vivo in a multiple sclerosis murine model. Proc. Natl. Acad. Sci. U. S. A. 114, E6982–E6991.

Guglielmetti, C., Veraart, J., Roelant, E., Mai, Z., Daans, J., Van Audekerke, J., Naeyaert, M., Vanhoutte, G., Delgado, Y.P.R., Praet, J., Fieremans, E., Ponsaerts, P., Sijbers, J., Van der Linden, A., Verhoye, M., 2016b. Diffusion kurtosis imaging probes cortical alterations and white matter pathology following cuprizone induced demyelination and spontaneous remyelination. Neuroimage 125, 363–377.

He, Q., Ma, Y., Fan, S., Shao, H., Sheth, V., Bydder, G.M., Du, J., 2017. Direct magnitude and phase imaging of myelin using ultrashort echo time (UTE) pulse sequences: a feasibility study. Magn. Reson. Imaging 39, 194–199.

Heath, F., Hurley, S.A., Johansen-Berg, H., Sampaio-Baptista, C., 2018. Advances in noninvasive myelin imaging. Dev. Neurobiol. 78, 136–151.

Hibbits, N., Pannu, R., Wu, T.J., Armstrong, R.C., 2009. Cuprizone demyelination of the corpus callosum in mice correlates with altered social interaction and impaired bilateral sensorimotor coordination. ASN Neuro 1.

Hodgson, R.J., Evans, R., Wright, P., Grainger, A.J., O'Connor, P.J., Helliwell, P., McGonagle, D., Emery, P., Robson, M.D., 2011. Quantitative magnetization transfer ultrashort echo time imaging of the Achilles tendon. Magn. Reson. Med. 65, 1372–1376.

Horch, R.A., Gore, J.C., Does, M.D., 2011. Origins of the ultrashort-T2 1H NMR signals in myelinated nerve: a direct measure of myelin content? Magn. Reson. Med. 66, 24–31.

Jelescu, I.O., Zurek, M., Winters, K.V., Veraart, J., Rajaratnam, A., Kim, N.S., Babb, J.S., Shepherd, T.M., Novikov, D.S., Kim, S.G., Fieremans, E., 2016. In vivo quantification of demyelination and recovery using compartment-specific diffusion MRI metrics validated by electron microscopy. Neuroimage 132, 104–114.

Khodanovich, M.Y., Sorokina, I.V., Glazacheva, V.Y., Akulov, A.E., Nemirovich-Danchenko, N.M., Romashchenko, A.V., Tolstikova, T.G., Mustafina, L.R., Yarnykh, V.L., 2017. Histological validation of fast macromolecular proton fraction mapping as a quantitative myelin imaging method in the cuprizone demyelination model. Sci. Rep. 7, 46686.

Kipp, M., Clarner, T., Dang, J., Copray, S., Beyer, C., 2009. The cuprizone animal model: new insights into an old story. Acta Neuropathol. 118, 723–736.

Koutsoudaki, P.N., Skripuletz, T., Gudi, V., Moharregh-Khiabani, D., Hildebrandt, H., Trebst, C., Stangel, M., 2009. Demyelination of the hippocampus is prominent in the cuprizone model. Neurosci. Lett. 451, 83–88.

Kutzelnigg, A., Lassmann, H., 2006. Cortical demyelination in multiple sclerosis: a substrate for cognitive deficits? J. Neurol. Sci. 245, 123–126.

Kutzelnigg, A., Lucchinetti, C.F., Stadelmann, C., Bruck, W., Rauschka, H., Bergmann, M., Schmidbauer, M., Parisi, J.E., Lassmann, H., 2005. Cortical demyelination and diffuse white matter injury in multiple sclerosis. Brain 128, 2705–2712.

Larson, P.E., Gurney, P.T., Nayak, K., Gold, G.E., Pauly, J.M., Nishimura, D.G., 2006. Designing long-T2 suppression pulses for ultrashort echo time imaging. Magn. Reson. Med. 56, 94–103.
Larson, P.Z., Gurney, P.T., Nishimura, D.G., 2008. Anisotropic field-of-views in radial imaging. IEEE Trans. Med. Imaging 27, 47–57.
Laule, C., Vavasour, I.M., Kolind, S.H., Li, D.K., Traboulsee, T.L., Moore, G.R., MacKay, A.L., 2007. Magnetic resonance imaging of myelin. Neurotherapeutics 4, 460–484.
Love, S., 2006. Demyelinating diseases. J. Clin. Pathol. 59, 1151–1159.
Lucchinetti, C., Bruck, W., Parisi, J., Scheithauer, B., Rodriguez, M., Lassmann, H., 2000. Heterogeneity of multiple sclerosis lesions: implications for the pathogenesis of demyelination. Ann. Neurol. 47, 707–717.
Lucchinetti, C.F., Popescu, B.F., Bunyan, R.F., Moll, N.M., Roemer, S.F., Lassmann, H., Bruck, W., Parisi, J.E., Scheithauer, B.W., Giannini, C., Weigand, S.D., Mandrekar, J., Ransohoff, R.M., 2011. Inflammatory cortical demyelination in early multiple sclerosis. N. Engl. J. Med. 365, 2188–2197.
Matsushima, G.K., Morell, P., 2001. The neurotoxicant, cuprizone, as a model to study demyelination and remyelination in the central nervous system. Brain Pathol. 11, 107–116.
Merkler, D., Boretius, S., Stadelmann, C., Ernsting, T., Michaelis, T., Frahm, J., Bruck, W., 2005. Multicontrast MRI of remyelination in the central nervous system. NMR Biomed. 18, 395–403.
Nathoo, N., Yong, V.W., Dunn, J.F., 2014. Understanding disease processes in multiple sclerosis through magnetic resonance imaging studies in animal models. Neuroimage Clin. 4, 743–756.
Norkute, A., Hieble, A., Braun, A., Johann, S., Clarner, T., Baumgartner, W., Beyer, C., Kipp, M., 2009. Cuprizone treatment induces demyelination and astrocytosis in the mouse hippocampus. J. Neurosci. Res. 87, 1343–1355.
Ontaneda, D., Fox, R.J., 2017. Imaging as an outcome measure in multiple sclerosis. Neurotherapeutics 14, 24–34.
Petiet, A., Aigrot, M.S., Stankoff, B., 2016. Gray and white matter demyelination and remyelination detected with multimodal quantitative MRI analysis at 11.7T in a chronic mouse model of multiple sclerosis. Front. Neurosci. 10, 491.
Piedzia, W., Jasinski, K., Kalita, K., Tomanek, B., Weglarz, W.P., 2014. White and gray matter contrast enhancement in MR images of the mouse brain in vivo using IR UTE with a cryo-coil at 9.4 T. J. Neurosci. Methods 232, 30–35.
Plemel, J.R., Liu, W.Q., Yong, V.W., 2017. Remyelination therapies: a new direction and challenge in multiple sclerosis. Nat. Rev. Drug Discov. 16, 617–634.
Popescu, B.F., Lucchinetti, C.F., 2012. Pathology of demyelinating diseases. Annu. Rev. Pathol. 7, 185–217.
Praet, J., Guglielmetti, C., Berneman, Z., Van der Linden, A., Ponsaerts, P., 2014. Cellular and molecular neuropathology of the cuprizone mouse model: clinical relevance for multiple sclerosis. Neurosci. Biobehav. Rev. 47, 485–505.
Reich, D.S., Lucchinetti, C.F., Calabresi, P.A., 2018. Multiple sclerosis. N. Engl. J. Med. 378, 169–180.
Robson, M.D., Gatehouse, P.D., Bydder, M., Bydder, G.M., 2003. Magnetic resonance: an introduction to ultrashort TE (UTE) imaging. J. Comput. Assist. Tomogr. 27, 825–846.
Savaskan, N.E., Weinmann, O., Heimrich, B., Eyupoglu, I.Y., 2009. High resolution neurochemical gold staining method for myelin in peripheral and central nervous system at the light- and electron-microscopic level. Cell Tissue Res. 337, 213–221.
Schmued, L., Bowyer, J., Cozart, M., Heard, D., Binienda, Z., Paule, M., 2008. Introducing Black-Gold II, a highly soluble gold phosphate complex with several unique advantages for the histochemical localization of myelin. Brain Res. 1229, 210–217.
Sheth, V., Shao, H., Chen, J., Vandenberg, S., Corey-Bloom, J., Bydder, G.M., Du, J., 2016. Magnetic resonance imaging of myelin using ultrashort Echo time (UTE) pulse sequences: phantom, specimen, volunteer and multiple sclerosis patient studies. Neuroimage 136, 37–44.
Sheth, V.R., Fan, S., He, Q., Ma, Y., Annese, J., Switzer, R., Corey-Bloom, J., Bydder, G.M., Du, J., 2017. Inversion recovery ultrashort echo time magnetic resonance imaging: a method for simultaneous direct detection of myelin and high signal demonstration of iron deposition in the brain - a feasibility study. Magn. Reson. Imaging 38, 87–94.
Skripuletz, T., Bussmann, J.H., Gudi, V., Koutsoudaki, P.N., Pul, R., Moharregh-Khiabani, D., Lindner, M., Stangel, M., 2010. Cerebellar cortical demyelination in the murine cuprizone model. Brain Pathol. 20, 301–312.
Skripuletz, T., Lindner, M., Kotsiari, A., Garde, N., Fokuhl, J., Linsmeier, F., Trebst, C., Stangel, M., 2008. Cortical demyelination is prominent in the murine cuprizone model and is strain-dependent. Am. J. Pathol. 172, 1053–1061.
Soustelle, L., Antal, M.C., Lamy, J., Rousseau, F., Armspach, J.P., Loureiro de Sousa, P., 2019. Correlations of quantitative MRI metrics with myelin basic protein (MBP) staining in a murine model of demyelination. NMR Biomed. e4116.
Stadelmann, C., Albert, M., Wegner, C., Bruck, W., 2008. Cortical pathology in multiple sclerosis. Curr. Opin. Neurol. 21, 229–234.
Steelman, A.J., Thompson, J.P., Li, J., 2012. Demyelination and remyelination in anatomically distinct regions of the corpus callosum following cuprizone intoxication. Neurosci. Res. 72, 32–42.
Syha, R., Springer, F., Grozinger, G., Wurslin, C., Ipach, I., Ketelsen, D., Schabel, C., Gebhard, H., Hein, T., Martirosian, P., Schick, F., Claussen, C.D., Grosse, U., 2014. Short-term exercise-induced changes in hydration state of healthy Achilles tendons can be visualized by effects of off-resonant radiofrequency saturation in a three-dimensional ultrashort echo time MRI sequence applied at 3 Tesla. J. Magn. Reson. Imaging 40, 1400–1407.
Tagge, I., O'Connor, A., Chaudhary, P., Pollaro, J., Berlow, Y., Chalupsky, M., Bourdette, D., Woltjer, R., Johnson, M., Rooney, W., 2016. Spatio-temporal patterns of demyelination and remyelination in the cuprizone mouse model. PLoS One 11, e0152480.
Thiessen, J.D., Zhang, Y., Zhang, H., Wang, L., Buist, R., Del Bigio, M.R., Kong, J., Li, X.M., Martin, M., 2013. Quantitative MRI and ultrastructural examination of the cuprizone mouse model of demyelination. NMR Biomed. 26, 1562–1581.
Torkildsen, O., Brunborg, L.A., Myhr, K.M., Bo, L., 2008. The cuprizone model for demyelination. Acta Neurol. Scand. Suppl. 188, 72–76.
Traboulsee, A., Simon, J.H., Stone, L., Fisher, E., Jones, D.E., Malhotra, A., Newsome, S.D., Oh, J., Reich, D.S., Richert, N., Rammohan, K., Khan, O., Radue, E.W., Ford, C., Halper, J., Li, D., 2016. Revised recommendations of the consortium of MS centers task force for a standardized MRI protocol and clinical guidelines for the diagnosis and follow-up of multiple sclerosis. AJNR Am. J. Neuroradiol. 37, 394–401.
Turati, L., Moscatelli, M., Mastropietro, A., Dowell, N.G., Zucca, I., Erbetta, A., Cordiglieri, C., Brenna, G., Bianchi, B., Mantegazza, R., Cercignani, M., Baggi, F., Minati, L., 2015. In vivo quantitative magnetization transfer imaging correlates with histology during de- and remyelination in cuprizone-treated mice. NMR Biomed. 28, 327–337.
van Gelderen, P., de Zwart, J.A., Lee, J., Sati, P., Reich, D.S., Duyn, J.H., 2012. Nonexponential T(2) decay in white matter. Magn. Reson. Med. 67, 110–117.
Wei, H., Cao, P., Bischof, A., Henry, R.G., Larson, P.E.Z., Liu, C., 2018. MRI gradient-echo phase contrast of the brain at ultra-short TE with off-resonance saturation. Neuroimage 175, 1–11.
Wilhelm, M.J., Ong, H.H., Wehrli, S.L., Li, C., Tsai, P.H., Hackney, D.B., Wehrli, F.W., 2012. Direct magnetic resonance detection of myelin and prospects for quantitative imaging of myelin density. Proc. Natl. Acad. Sci. U. S. A. 109, 9605–9610.
Wu, Q.Z., Yang, Q., Cate, H.S., Kemper, D., Binder, M., Wang, H.X., Fang, K., Quick, M.J., Marriott, M., Kilpatrick, T.J., Egan, G.F., 2008. MRI identification of the rostral-caudal pattern of pathology within the corpus callosum in the cuprizone mouse model. J. Magn. Reson. Imaging 27, 446–453.
Xie, M., Tobin, J.E., Budde, M.D., Chen, C.I., Trinkaus, K., Cross, A.H., McDaniel, D.P., Song, S.K., Armstrong, R.C., 2010. Rostrocaudal analysis of corpus callosum demyelination and axon damage across disease stages refines diffusion tensor imaging correlations with pathological features. J. Neuropathol. Exp. Neurol. 69, 704–716.
Zaaraoui, W., Deloire, M., Merle, M., Girard, C., Raffard, G., Biran, M., Inglese, M., Petry, K.G., Gonen, O., Brochet, B., Franconi, J.M., Dousset, V., 2008. Monitoring demyelination and remyelination by magnetization transfer imaging in the mouse brain at 9.4 T. Magma 21, 357–362.